Correlations between the Growth Mechanism and Corrosion Resistance of Plasma Electrolytic Oxidation Coatings on AZ31B Magnesium Alloy

Yujie Wang[*], *Peng Zhang, Yunhui Du, Weiyi Zhang and Haitao Cao*

School of Mechanical, Electronic and Control Engineering, Beijing Jiaotong University, Beijing 100044, China
[*]E-mail: yujie_wendy@126.com

In the present work, plasma electrolytic oxidation (PEO) coatings with different microstructures were fabricated on AZ31B magnesium alloy. The thickness, morphology, phase composition and elemental distribution of the obtained coatings were characterized by X-ray diffraction (XRD), scanning electron microscopy (SEM), and energy dispersive spectroscopy (EDS). The corrosion behaviors of PEO coatings were measured by potentiodynamic polarization curves and electrochemical impedance spectroscopy (EIS). The results show that a composite dielectric coating is obtained with similar contents of MgO and MgF_2 (MgO-MgF_2 coating). During the discharge in the PEO process, by taking advantage of these two dielectrics' electrical performance and physical properties to influence dielectric breakdown, and utilizing the effect of blocking and heating in the two dielectrics, the molten materials ejected from the discharge channels decrease and more remains in the discharge channels; therefore, the thickness of the compact layer of the MgO-MgF_2 coating increases. Consequently, the coating thickness is approximately 3.5 μm, which is twice that of the coating with MgO as the main component (MgO coating). Furthermore, the results of electrochemical experiments demonstrate that the corrosion potential of the MgO-MgF_2 coating is 0.91 V larger than that of the MgO coating. As evaluated by EIS, the impedance of the inner compact layer is increased by more than 5 times from 7.652×10^5 $\Omega \cdot cm^2$ for the MgO coating to 4.933×10^6 $\Omega \cdot cm^2$ for the MgO-MgF_2 coating. These results indicate that the growth mechanism of the MgO-MgF_2 coating can increase the thickness of the compact layer and effectively improve the corrosion resistance.

1. INTRODUCTION

Magnesium alloys are one of the most frequently used materials in various industries including automobile, electronics, aerospace, and biodegradable implants due to their low density, high specific

strength, good machinability, excellent dimensional stability and damping capacity [1-4]. Nevertheless, magnesium alloys' susceptibility to corrosion seriously restricts their widespread application. Therefore, appropriate surface treatment technologies are greatly appealing to improve the corrosion resistance of magnesium alloys.

Plasma electrolytic oxidation (PEO), also known as micro-arc oxidation, is an effective method to produce a ceramic coating of high hardness and good corrosion resistance on valve metals (Al, Mg, and Ti) and their alloys [5-6]. However, several studies found that during the discharge of the PEO process, the energy generated by the dielectric breakdown causes a strong discharge pressure in the discharge channels [7]. Due to the great pressure, the molten products are ejected from discharge channels into the electrolyte [8-9]. Under this influence, conventional PEO coatings have a porous microstructure and the compact layer is thin, which significantly restricts the improvement in the corrosion resistance of substrates.

Recently, numerous analytical studies have been applied to enhance the corrosion resistance of PEO coatings through the optimization of process parameters [10-11], use of additives such as rare-earth metals [12-13], and the utilization of composition techniques including spraying [14], laser surface melting [15], sol-gel [16] and chemical plating [17-18]. However, most studies have mainly focused on improvements in the corrosion resistance by sealing or shrinking cavities on PEO coatings [19-20]. Studies on improving corrosion resistance of PEO coatings by increasing the thickness of the compact layer and providing an effective barrier towards corrosive species have not yet been systematically reported in the literature [21-22]. Furthermore, research on the discharge effects and growth mechanisms of PEO coatings needs to be conducted.

Hence, this study is based upon the relation of the growth mechanism and the microstructure and corrosion resistance of PEO coatings to reduce the ejection of molten material and increase the thickness of the compact layer by adjusting the phase contents of PEO coatings and utilizing the effects of the electrical performance and physical properties on the dielectric discharge. In addition, valuable guidance for further improving the anticorrosion properties of PEO coatings is provided. Therefore, it is necessary to better understand the growth mechanisms and corrosion properties of PEO coatings.

2. EXPERIMENTAL

2.1 Preparation of PEO coatings

The AZ31B Mg alloy (mass fraction: Al 2.5~3.5%, Zn 0.6~1.4%, Mn 0.2~1.0%, Si 0.1%, Cu 0.01%, Fe 0.005%, Ni 0.005%, Mg balance) samples were cut into 10 mm × 10 mm × 5 mm and polished with 600–2000 grit SiC sandpapers. Then, the samples were cleaned ultrasonically in acetone and distilled water and finally dried in air at room temperature. The PEO treatment device includes a 5 kW AC power supply unit, a 20 L stainless steel electrolyte container with an O_2 spray nozzle for stirring the electrolyte, and an external cooling system.

The PEO treatment was performed at a constant voltage of 130 V for 7 mins with a frequency of 50 Hz; the duty cycle was fixed at 50%. Samples were subjected to the PEO process in an electrolyte

consisting of potassium fluoride (KF) and potassium hydroxide (KOH). First, 20 g/L KOH was used as the base electrolyte; then, 20 g/L and 70 g/L KF were added to the base electrolyte and are referred to as E1 and E2 electrolytes, respectively. The O_2 was bubbled into the electrolyte at a rate of 0.01 L/s, and the electrolyte temperature was maintained below 40°C using a cooling system to prevent evaporation of the electrolyte during the PEO process.

2.2 Characterization of PEO coatings

The phase composition of the PEO coatings was examined via X-ray diffraction (XRD, BDX3300) with Cu K_α radiation at 40 kV, using a scan rate of 1°/min over a 2θ range from 20° to 70°. The morphology and elemental analysis of these coatings were observed using scanning electron microscopy (SEM, JSM-6510) equipped with energy dispersive spectrometry (EDS), and the thickness of the coatings was measured by the cross-section SEM observations.

The corrosion resistance of the bare and PEO coatings was evaluated via potentiodynamic polarization experiments and electrochemical impedance spectroscopy (EIS) measurements on an electrochemical workstation (CHI660E) in a 3.5 wt. % NaCl aqueous solution at 22°C. A conventional three-electrode cell with the specimen as the working electrode, a platinum plate as the counter electrode and a saturated calomel electrode (SCE) as the reference electrode. The exposed surface area of the specimens was 1 cm^2. After the electrochemical testing system became stable (approximately 30 min), the EIS measurements were conducted over a frequency range of 100 kHz to 10 mHz with a perturbation amplitude of 5 mV. Zview software was used for the data fitting of impedance spectra. Additionally, the potentiodynamic polarization curves were scanned from -2.5 V to 0 V at a scanning rate of 0.5 mV/s.

3. RESULTS AND DISCUSSION

3.1 Phase and chemical composition

The XRD patterns of the PEO coatings obtained in E1 and E2 electrolytes are shown in Figure 1. According to the XRD patterns, all oxidized coatings are mainly composed of magnesium oxide (MgO) and magnesium fluoride (MgF_2) phases, indicating that both the Mg alloy and electrolyte ions participate in the plasma electrolytic oxidation reaction. The possible reactions that occur during the PEO process are as follows [23-24]:

$$Mg \rightarrow Mg^{2+} + 2e^-$$

(1)

$$2OH^- \rightarrow O^{2+} + H_2O$$

(2)

$$KF \rightarrow K^+ + F^-$$

(3)

$$Mg^{2+} + 2F^- \rightarrow MgF_2$$

(4)

$$Mg^{2+} + O^{2-} \rightarrow MgO$$

(5)

$$Mg^{2+} + 2OH^- \rightarrow Mg(OH)_2$$

(6)

$$Mg(OH)_2 \rightarrow MgO + H_2O$$

(7)

As the oxidation proceeds, Mg^{2+} ions and some anions in the electrolyte such as OH^- and F^- migrate to the coating/electrolyte interface and react in the discharge channels under the effects of strong electric fields (approximately 10^6 to 10^8 V/m), leading to the formation of MgO and MgF_2 phases[25-26].

The XRD patterns in Figure 1 further demonstrate that both of the PEO coatings have a high intensity peak of MgO, while a clear difference in the intensities of the peaks for MgF_2 between the samples from E1 and E2 electrolytes is observed. More concretely, the XRD results reveal low intensity peaks of MgF_2 in the sample from the E1 electrolyte, and the MgF_2 peak intensity is stronger for the sample coated in the E2 electrolyte. This result might be attributed to the content ratios of KOH and KF being different in the E1 and E2 electrolytes. As mentioned before, KOH solutions provide OH^- for the reaction with Mg^{2+} and form MgO, while KF solutions offer F^- for the formation of MgF_2. Compared with the E1 electrolyte, the E2 electrolyte has a high proportion of KF, and more F^- ions participate in the coating formation.
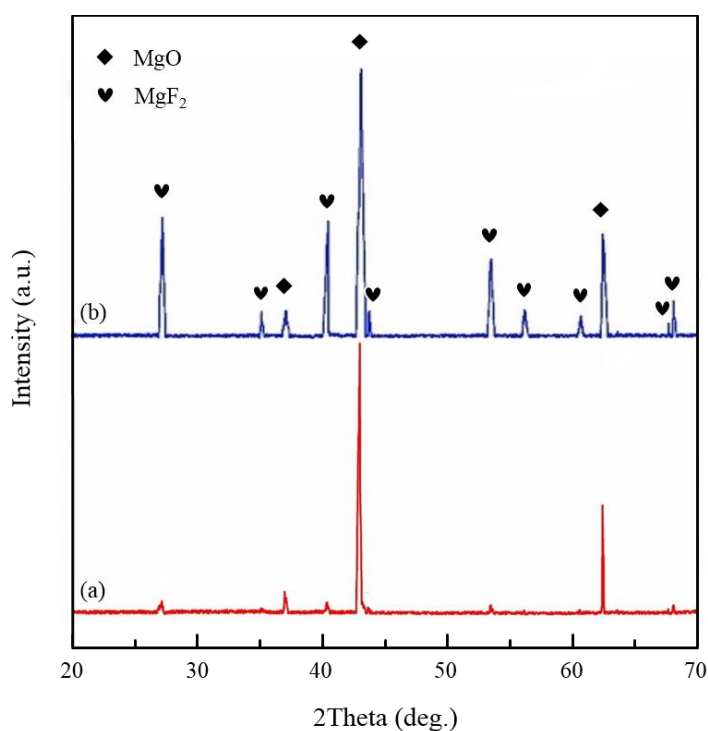

Figure 1. X-ray diffraction patterns of PEO coatings formed in: (a) the E1 electrolyte and (b) E2 electrolyte

To accurately analyze the XRD results, the phase contents of MgO and MgF_2 for different coatings are obtained by using the matrix-flushing method (number-K method) and are calculated by equations (1)-(2) [27]:

$$\frac{X_i}{X_f} = \frac{I_i}{I_f} \cdot \frac{K_f}{K_i} \tag{1}$$

$$\begin{cases} K_f = \left(\dfrac{I_f}{I_{cor}}\right)_{50/50} \\ K_i = \left(\dfrac{I_i}{I_{cor}}\right)_{50/50} \end{cases} \tag{2}$$

where X_i and X_f are the mass fractions of component i and component f, respectively; I_i and I_f are the intensities of the strongest diffraction peak of substance i and substance f, respectively; I_{cor} is the intensity of the strongest diffraction peak of corundum(α-Al_2O_3); and the coefficients K_f and K_i are the diffraction intensity ratios obtained by mixing component f and component i with α-Al_2O_3 at a mass ratio of 1:1, respectively.

By using equations (1) and (2), the results for the phase contents of PEO coatings produced from E1 and E2 electrolytes are shown in Figure 2. The contents of MgO and MgF_2 exhibit large differences between samples. For the PEO coating prepared in the E1 electrolyte, the mass fractions of MgO and MgF_2 are 90.96% and 9.04%, respectively. On the other hand, the mass ratio of these two phases is close to 1:1 for the sample formed in the E2 electrolyte. As the main crystal phases of the PEO coatings treated in the E1 and E2 electrolytes are MgO and MgO-MgF_2, the coatings obtained from these two electrolytes in this work are termed as the MgO coating and MgO-MgF_2 coating, respectively.
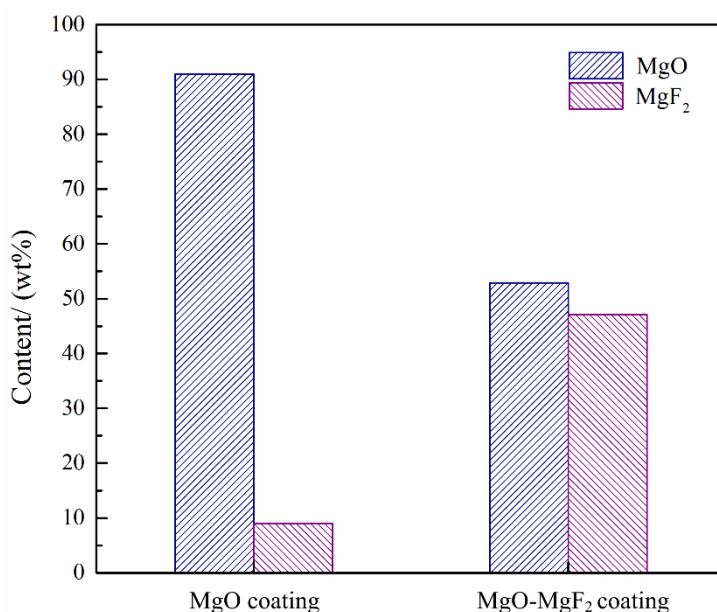

Figure 2. Quantitative phase analysis results for the PEO coatings on AZ31B magnesium alloy

3.2 Structural analyses of PEO coatings

The cross-section images of the MgO and MgO-MgF$_2$ coatings are presented in Figure 3. As is seen from the cross-sectional morphologies, the thickness of the PEO coatings is relatively uniform, and the fabricated coatings can be generally divided into two different regions: an inner compact layer and an outer loose layer with discharge pores.
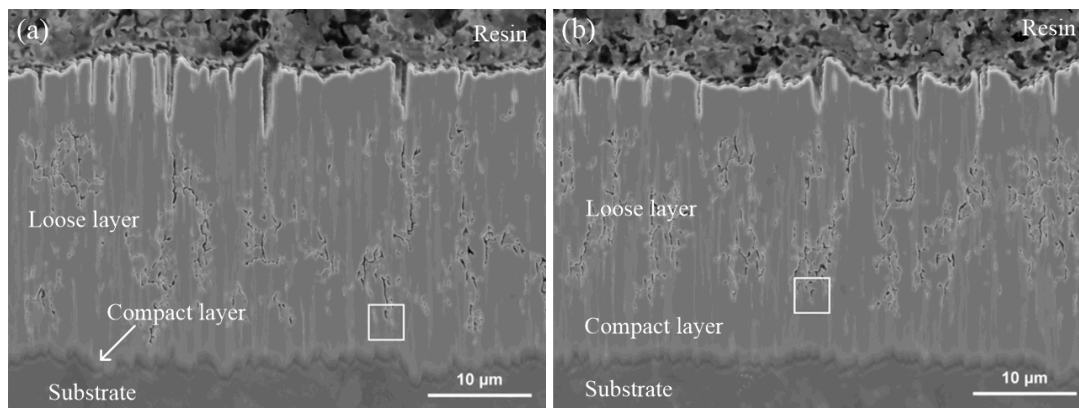

Figure 3. SEM cross-sectional micrographs of the (a) MgO coating and (b) MgO-MgF$_2$ coating

As the most distinguishing features, the structure of a PEO coating is closely related to the breakdown effects. In the initial stage of micro-arc discharge, a relatively low sparking voltage develops on the samples and uniformly breakdowns the oxide coating. This behavior does not cause a strong discharge energy input through the discharge channels, and the eruption of molten products are not intense. Based on this observation, the molten products can effectively block the discharge channels, and the coating is relatively compact[28].However, with further processing time and the aggravation of micro-arc oxidation reactions, the micro-arc discharge becomes intensified, and the breakdown of the PEO coating is also strengthened, resulting in a larger discharge energy generated in the discharge channels. Therefore, abundant molten materials are ejected out from the discharge channels, and the growth of the coating is no longer compact as before. Figure 3 also reveals that the thickness of the inner compact layer is limited.

Apart from the influence of the discharge intensity on the coating's formation, the electrical performance, such as the dielectric constant, influences the breakdown effects and contributes to the growth of the PEO coating as well[29]. According to our previous work, the XRD results show that the MgO-MgF$_2$ coating is composed of MgO and MgF$_2$ in similar amounts, and there is a difference in the dielectric constants between MgO (9.7) and MgF$_2$ (5.45) [30]. Because the larger dielectric constant of MgO provides better insulation, MgF$_2$, with a smaller dielectric constant, is prone to breakdown before the MgO dielectric and lose its insulating properties. Under this influence, during the discharge of the PEO process, the dielectric discharge initially occurs at MgF$_2$, and then, when the breakdown energy is large enough, the breakdown of MgO happens subsequently. Apparently, compared with the MgO coating, which is composed primarily of MgO and has a larger dielectric constant, the nonsimultaneous breakdowns of MgF$_2$ and MgO inside the discharge channels of the MgO-MgF$_2$ coating make the discharge energy relatively scattered. Therefore, the micro-arc discharge process of the MgO-MgF$_2$

coating becomes relatively mild, and the discharge intensity is reduced. In addition, the eruption of molten materials is weakened, and more of them remain in the discharge channels so that the thickness of the compact layer for the MgO-MgF$_2$ coating can be significantly increased. Figure 3 shows the thicknesses of the compact layers on the MgO and MgO-MgF$_2$ coatings are 1.5 μm and 3.5 μm, respectively.

Figure 3 further demonstrates that both the MgO coating and MgO-MgF$_2$ coating have a porous morphology on the outer layer of the coatings. Furthermore, the surfaces of these coatings present a "volcano orifice" topography, as illustrated in Figure 4. This structure happens due to intense discharge and strong ejection of molten materials based on the energy induced by the electron avalanche effect, which corresponds to the breakdown feature of PEO coatings [31-32]. In addition, the absence of the loose layer and a volcano-like microstructure in the PEO coatings supports the facts that the microstructure and morphology are closely related to the discharge effects of and growth mechanism for the coatings, and the strong eruption of molten materials is not conducive to the thickening of the compact layer.
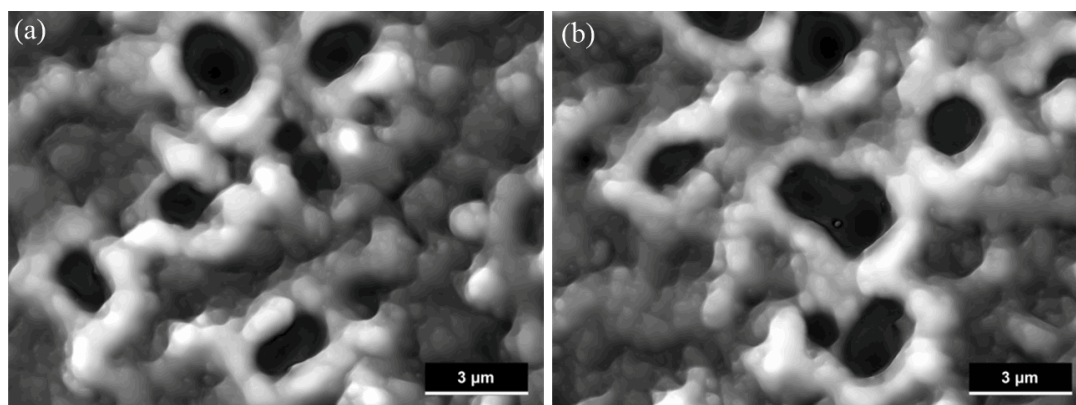

Figure 4. SEM surface morphologies of the (a) MgO coating and (b) MgO-MgF$_2$ coating

3.3 Growth mechanisms of PEO coatings

Plasma electrolytic oxidation is a cyclic process of "forming →breakdown →melting →ejecting →depositing →reforming". The above processes, which occur in the discharge channels, have great influences on the coating formation and its properties [33].To further analyze the growth mechanism of PEO coatings and investigate the elemental composition of the obtained coatings, the discharge channels of the MgO coating and MgO-MgF$_2$ coating in the transition zone between the inner compact layer and the outer loose layer are magnified. In addition, these transition zones were investigated by EDS to exhibit the element distributions around the discharged channels. EDS detects the common elements oxygen and fluorine, which present the main phases of MgO and MgF$_2$, respectively. The results are shown in Figure 5.

It can be noted from Figure 5 that MgO and MgF$_2$ are interlaced and distributed throughout the cross-section of the MgO-MgF$_2$ coating. According to our previous works, during the PEO process, the reaction particles from the electrolyte and matrix enter the discharge channels and participate in the

coating formation. Then, MgO and MgF$_2$ are obtained in the discharge channels via complex reactions involving electrochemistry, thermochemistry and plasma chemical reactions and are accompanied by an energy release. Subsequently, the reaction products are melted and ejected from the discharge channels into the electrolyte. Research has shown that in the above reaction processes, the microstructures, dielectric and physical properties of the dielectrics influence the breakdown effects and growth mechanism of the MgO-MgF$_2$ coating. A schematic illustration of discharge models is shown in Figure 6.
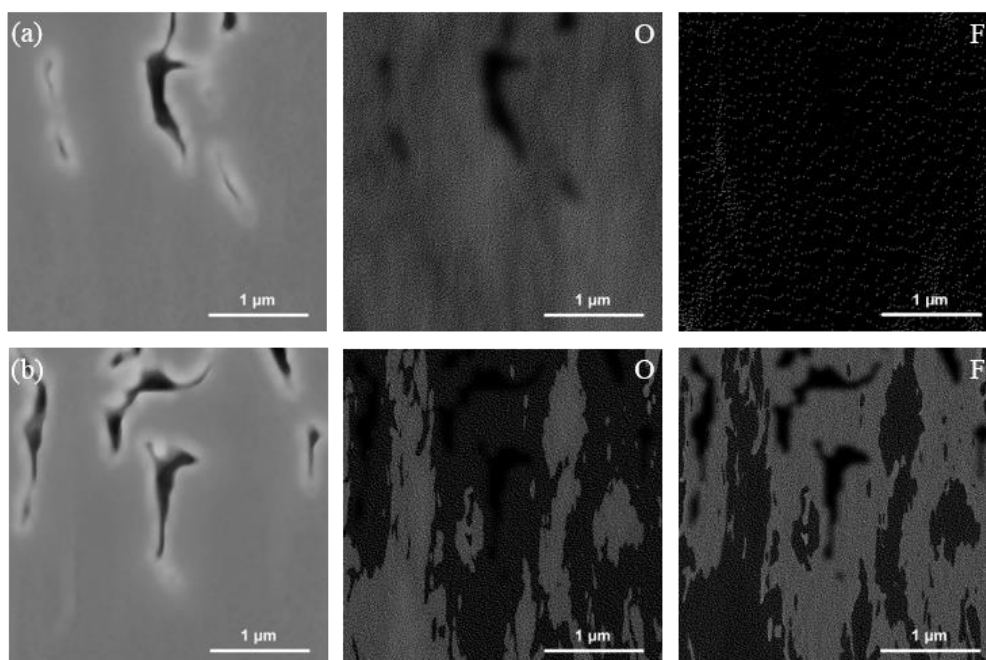

Figure 5. Cross-sectional magnified micrographs of the (a) MgO coating and (b) MgO-MgF$_2$ coating around the discharge channels from Figure 3 (white frame) and the corresponding EDS maps of O and F

When the MgO-MgF$_2$ coating is broken down, discharges are prone to occur at the MgF$_2$ dielectric with a low dielectric constant and to favor the molten state. Meanwhile, the MgO dielectric, with a high dielectric constant, does not breakdown yet because of its better insulation. Additionally, MgO does not melt yet because it has a higher melting point (2800°C) than MgF$_2$ (1266°C) [34]. Thus, the unmelted MgO, which is adjacent to the MgF$_2$ and does not breakdown yet, can block the eruption of molten MgF$_2$.

Meanwhile, the high energy and joule heat generated in the discharge channels when MgF$_2$ is broken down diffuses and transmits to the adjacent dielectric MgO. More concretely, the energy accumulated in the discharge process of MgF$_2$ will be injected into the discharge point along the discharge channels. This action helps to sufficiently preheat MgO and supply the energy required for the dielectric's subsequent breakdown [35]. Based on this concept, the subsequent breakdown of MgO is more likely to occur. Under preheating conditions, when the MgO dielectric obtains enough electron kinetic energy, the electron avalanche occurs without accumulating large energy and causes the

breakdown of MgO. As a result, the molten eruption is weakened due to the relatively mild breakdown effects, which helps to thicken the inner compact layer.
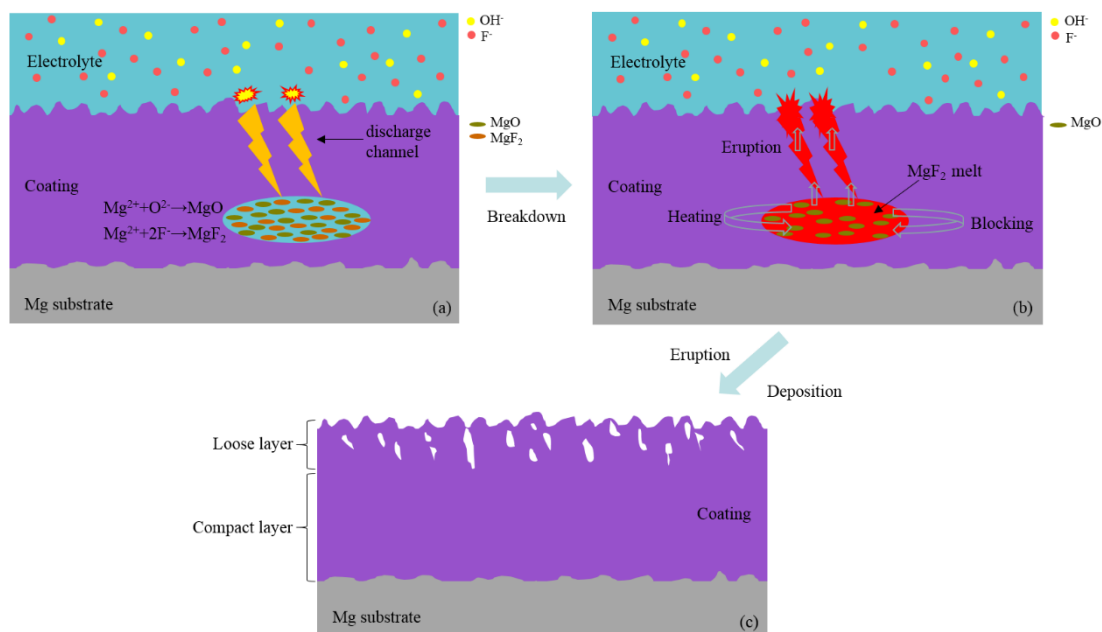

Figure 6. Schematic illustration of the discharge models for the MgO-MgF$_2$ coating

As for the MgO coating in Figure 5, there are a multitude of O elements in the discharge channels, while only a small number of F elements are scattered across the section. Hence, the interactions between blocking and heating for the above MgO-MgF$_2$ coating will be weakened. Because the heat released by the breakdown of MgF$_2$ cannot fully preheat the large amount of MgO in the discharge channels, more energy is needed to achieve the breakdown of MgO. With a stronger micro-arc discharge on the MgO dielectric, a larger electronic avalanche is generated, and leads to a great discharge pressure and intensive eruption [36-37]. In general, the growth mechanism for the MgO coating basically continues the traditional discharge mode, i.e., intensive discharge and strong eruption in the micro-arc oxidation process. Under this influence, compared with the MgO-MgF$_2$ coating, the eruption of molten materials with the MgO coating is intense, and just a small portion remains in the discharge channels. Therefore, the inner compact layer of the MgO coating is thinner, which corresponds to the cross-sectional morphology in Figure 3.

These discharge effects clearly play an important role in the coating growth mechanism. In Figure 5 and Figure 6, for the MgO-MgF$_2$ coating, the differences in dielectric constants and melting points between MgF$_2$ and MgO create favorable conditions for the breakdown effects and growth mechanism. The intensity of the discharge is decreased due to the nonsimultaneous breakdown of MgO and MgF$_2$, and the heat released by the molten MgF$_2$ results in the breakdown of MgO to occur without accumulating more discharge energy under the influences of the electric-thermal coupling field. At the same time, the interlaced microstructures of MgF$_2$ and MgO can be better utilize the effects of heating and blocking between the two dielectrics and reduce the strong avalanche breakdown. Thus, the eruption of molten materials is not intensive, and more molten materials remain in the discharge channels to

achieve the thickening of the inner compact layer of the MgO-MgF$_2$ coating, which can effectively protect the substrate from the corrosion medium.

3.4 Corrosion performance of PEO coatings

The potentiodynamic polarization curves obtained for the magnesium alloy, MgO coating, and MgO-MgF$_2$ coating in a 3.5 wt. % NaCl solution are shown in Figure 7. The corrosion potential (E_{coor}), corrosion current density (i_{coor}) and the anodic/cathodic Tafel slopes (β_a and β_c) obtained with the Tafel extrapolation method are displayed in Table 1. The polarization resistance (R_p) is calculated from the Stern-Geary equation [38].

$$R_p = \frac{\beta_a \beta_c}{2.303 i_{corr}(\beta_a + \beta_c)} \tag{3}$$

E_{coor}, i_{coor} and R_p are usually applied to characterize the corrosion performance of PEO coatings. In general, a large positive corrosion potential, low corrosion current density and high polarization resistance indicate superior anticorrosion properties [39-40]. In Table 1, the uncoated AZ31B shows the smallest corrosion potential (-1.909 V), highest corrosion current density (1.50×10^{-4} A/cm^2), and lowest polarization resistance (60.12 Ω·cm^2). While the PEO coatings provide resistances against the chemical attack of chloride ions and present larger corrosion potentials, lower corrosion current densities and higher polarization resistances than those of the substrate. Hence, the magnesium alloy becomes less vulnerable to corrosion after micro-arc oxidation treatments.
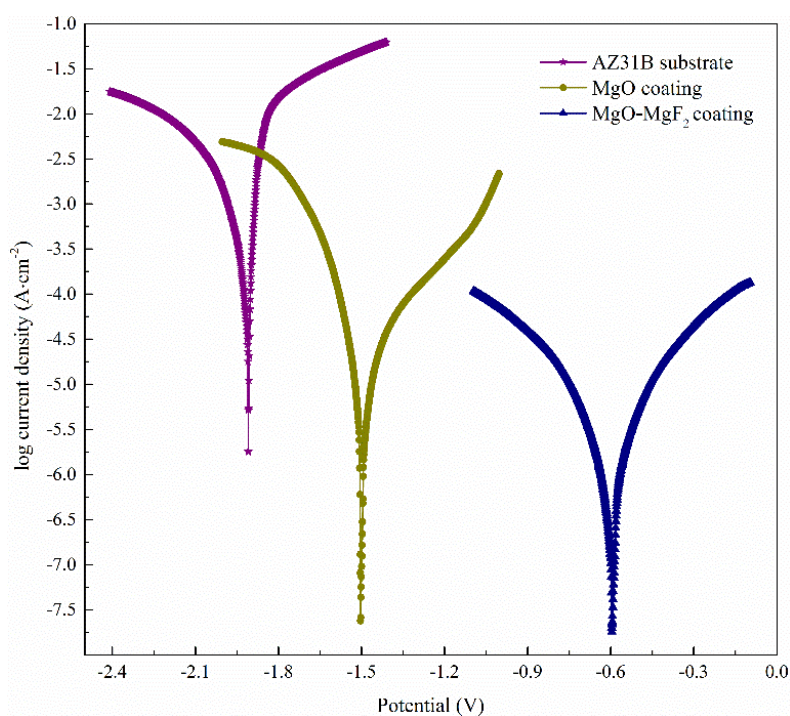

Figure 7. Potentiodynamic polarization curves of the bare alloy, MgO coating and MgO-MgF$_2$ coating in a 3.5 wt. % NaCl solution at 22°C

It can be further noted from the values of E_{coor} that the MgO-MgF$_2$ coating raises the corrosion potential by approximately + 1.313 V to a more positive value than that of the substrate, while the MgO coating does not improve the corrosion potential substantially more than that of the MgO-MgF$_2$ coating (406 mV). Furthermore, the i_{coor} of the MgO-MgF$_2$ coating is reduced by three orders of magnitude compared with that of the Mg alloy, and the value is one order of magnitude lower than that of the MgO coating. Additionally, the polarization resistance of the MgO-MgF$_2$ coating is estimated to reach $4.63 \times 10^4 \, \Omega \cdot cm^2$, which is more than 769 times the value of R_p for the Mg alloy substrate and approximately 15 times that of the MgO coating. All these data indicate that the MgO-MgF$_2$ coating exhibits the largest E_{coor}, smallest i_{coor} and highest R_p, suggesting that compared with the MgO coating, the MgO-MgF$_2$ coating can significantly decrease the thermodynamic tendency of corrosion occurrence and improve the chemical stability of the substrate, which protects the AZ31B Mg alloy more effectively [41].

Table 1. Analysis data of the potentiodynamic polarization curves of the substrate, MgO coating and MgO-MgF$_2$ coating

Sample	E_{coor} (V)	I_{coor} (A·cm^{-2})	β_a (mV/dec)	$\lvert\beta_c\rvert$ (mV/dec)	R_p (Ω·cm$^{2)}$)
Substrate	-1.909	1.50×10^{-4}	27	91	60.12
MgO coating	-1.503	4.96×10^{-6}	101	54	3.08×10^3
MgO-MgF$_2$ coating	-0.596	3.20×10^{-7}	61	77	4.63×10^4

To further analyze the corrosion performances, electrochemical impedance spectroscopy measurements are conducted for the MgO coating and MgO-MgF$_2$ coating, and Figure 8 shows the Bode-impedance plots and Bode-phase plots of these samples. According to Figure 8(a), the value of |Z| in the low-frequency range of the MgO-MgF$_2$ coating is significantly higher than that of the MgO coating, which demonstrates the better anticorrosion property of the MgO-MgF$_2$ coating on the Mg substrate [42]. It is well-known from electrochemical theory that the low-frequency range corresponds to the properties of the inner compact layer, while the high-frequency portion of the impedance spectrum reflects the properties of the outer loose layer [43-44]. The EIS plots reveal that the impedance of the inner compact layer is far greater than that of the outer loose layer. This result is due to the presence of micropores in the loose layer acting as transportation passages and letting corrosive ions penetrate through the coating [45], while the compact layer has nearly no micropores and can effectively suppress the diffusion of corrosive ions[46]. Meanwhile, the impedance of the compact layer of the MgO-MgF$_2$ coating is also significantly higher than that of the MgO coating because the thickness of the inner compact layer of the MgO-MgF$_2$ coating is greater. These findings illustrate that the MgO-MgF$_2$ coating can substantially enhance the corrosion resistance of the AZ31B Mg alloy, which is similar to observations reported by the literatures [47-48].

Figure 8(b) reveals that two time constants appear in the Bode-phase plots, which correspond to the double-layered structure of the PEO coatings [49]. Taking into account the microstructures and the Bode plots of the PEO coatings, the proposed equivalent circuit is provided in Figure 9 [50]. For the equivalent circuit of the coated samples, R_s represents the solution resistance, and R_{II} and R_{dI} correspond to the resistance of the outer loose layer and inner compact layer, respectively. Table 2 gives the results from the fitting of the electrochemical parameters of the equivalent circuit.
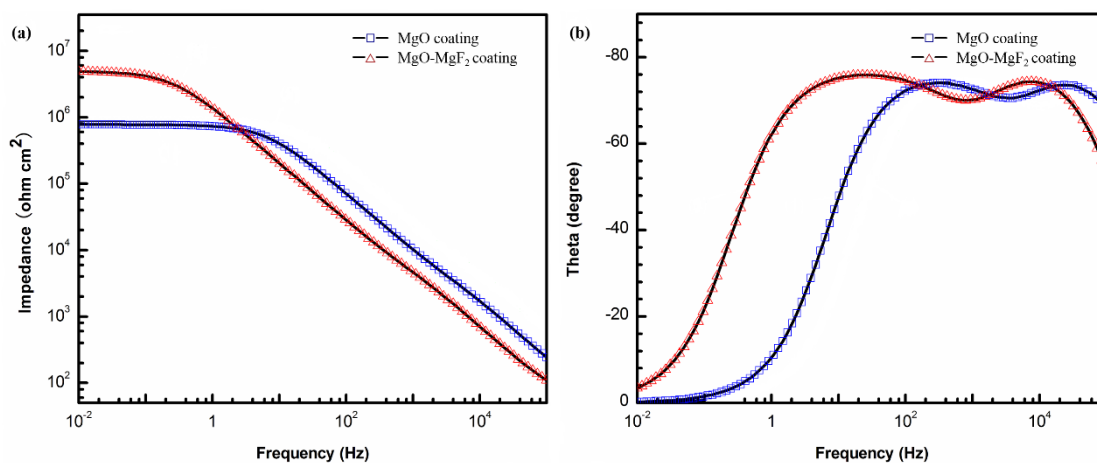

Figure 8. EIS plots of the MgO coating and MgO-MgF$_2$ coating: (a) Bode-impedance plots; (b) Bode-phase plots in a 3.5 wt. % NaCl solution at 22°C
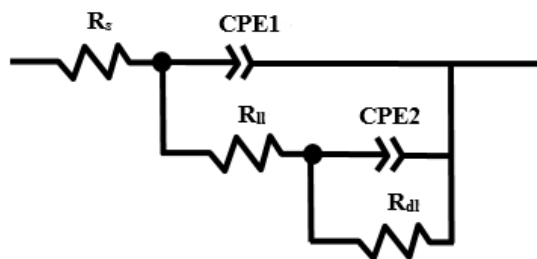

Figure 9. Equivalent circuit used for fitting the EIS data, Rs: solution resistance, R$_{II}$: outer loose layer resistance, CPE1: constant phase element of the outer loose layer, R$_{dI}$: inner compact layer resistance and CPE2: constant phase element of the inner compact layer

Table 2. Fitting results of the EIS plots for the MgO coating and MgO-MgF$_2$ coating

Sample	R_s ($\Omega \cdot cm^2$)	R_{II} ($\Omega \cdot cm^2$)	R_{dI} ($\Omega \cdot cm^2$)
MgO coating	48	10350	7.652×10^5
MgO-MgF$_2$ coating	51	13326	4.933×10^6

According to Table 2, the R_{II} of the MgO coating is basically the same as that of the MgO-MgF$_2$ coating, while the R_{dI} of the MgO coating and MgO-MgF$_2$ coating are approximately 1 to 2 orders of magnitude higher than the R_{II} of these coatings, indicating that the protection ability of the outer layer is extraordinarily restricted because the outer loose layer of the PEO coatings cannot block the corrosive medium or provide effective protection for the matrix. Thus, the effectiveness of the corrosion protection is mainly dependent upon the inner compact layer, because this layer decreases the penetration to the coating and prevents the substrate from contacting corrosive ions [51]. In addition, the R_{dI} values of the MgO coating and MgO-MgF$_2$ coating are 7.652×10^5 $\Omega \cdot cm^2$ and 4.933×10^6 $\Omega \cdot cm^2$, and the R_{dI} of the MgO-MgF$_2$ coating corresponds to the inner compact layer that is twice as thick as that of the MgO coating, as displayed in Figure 3. The data also confirms that the thicker the compact layer is, the more it can obstruct the diffusion of corrosive ions to the substrate and the better the corrosion resistance of the coating [52]. These results demonstrate that the MgO-MgF$_2$ coating, with a thicker inner compact layer, has a better corrosion resistance, and the EIS results are consistent with the potentiodynamic polarization measurement shown in Figure 7.

In general, the results obtained by the polarization data and by EIS tests both indicate that the corrosion resistance of the Mg substrate can be significantly enhanced by the MgO-MgF$_2$ coating due to the thicker inner compact layer, which offers more effective protection against corrosion. This approach is an effective way to improve the corrosion resistance of PEO coatings by reducing the eruption of molten materials and promoting the thickening of the compact layer.

4. CONCLUSIONS

Composite dielectric coatings obtained with similar contents of MgO and MgF$_2$ (MgO-MgF$_2$ coating) and with MgO as the main component (MgO coating) are prepared on the AZ31B magnesium alloy. The growth characteristics and corrosion resistance of the PEO coatings are investigated, and the main results are as follows:

(1) The thickness of the inner compact layer for the MgO-MgF$_2$ coating is approximately 3.5 μm, which is more than twice that of the MgO coating. The reason that the compact layer of the MgO-MgF$_2$ coating is significantly improved is that the differences in electrical performance and physical properties between the two phases develop the effects of blocking and heating during the process of dielectric breakdown and cause weaker eruptions of molten materials. Moreover, the interlaced microstructure of MgF$_2$ and MgO can better utilize the above interactions and promote the thickening of the inner compact layer.

(2) The results obtained from the potentiodynamic polarization tests show that corrosion potential of the MgO-MgF$_2$ coating is 0.907 V and 1.313 V larger than that of the MgO coating and bare Mg alloy, respectively. In addition, the impedance of the inner compact layer evaluated by EIS increases approximately 5 times from 7.652×10^5 $\Omega \cdot cm^2$ for the MgO coating to 4.933×10^6 $\Omega \cdot cm^2$ for the MgO-MgF$_2$ coating. Therefore, it can be concluded that the MgO-MgF$_2$ coating, with a thick inner compact layer, on the AZ31B Mg alloy can effectively improve the corrosion resistance.

References

1. L.J. Qu, M.Q. Li, M. Liu, E. Zhang and C. Ma, *J. Adv. Ceram.*, 2 (2013) 227.
2. Y.W. Song, K.H. Dong, D.Y. Shan and E.H. Han, *J. Magnes. Alloy.*, 1 (2013) 82.
3. L.R. Krishna, G. Poshal, A. Jyothirmayi and G. Sundararajan, *Mater. Des.*, 77 (2015) 6.
4. L.H. Li, T.S.N.S. Narayanan, Y.K. Kim, Y.M. Kong, G.S. Shin, S.K. Lyu, I.S. Park and M.H. Lee, *Int. J. Precis. Eng. Manuf.*, 15 (2014) 1625.
5. Z.X. Wang, W.G. Lv, J. Chen and S. Lu, *Rare Met.*, 32 (2013) 459.
6. Z.Z. Qiu, R. Wang, Y.S. Zhang, Y.F. Qu and X.H. Wu, *J. Mater. Eng. Perform.*, 24 (2015) 1483.
7. G. Sundararajan and L.R. Krishna, *Surf. Coat. Technol.*, 167 (2003) 269.
8. W.Y. Liu, Y. Liu, Y.H. Lin, Z. Zhang, S.B. Feng, M. Talha, Y.S. Shi and T.H. Shi, *Appl. Surf. Sci.*, 475 (2019) 645.
9. J. Liang, P.B. Srinivasan, C. Blawert and W. Dietzel, *Corrosion Sci.*, 51 (2009) 2483.
10. Y. Zhang, W. Fan, H.Q. Du and Y.W. Zhao, *Int. J. Electrochem. Sci.*, 12 (2017) 6788.
11. C.F. Xu, X.Y. Yan, H.W. Yang and H. Yan, *Int. J. Electrochem. Sci.*, 13 (2018) 3555.
12. M. Laleh, F. Kargar and A.S. Rouhaghdam, *J. Coat. Technol. Res.*, 8 (2011) 765.
13. K.M. Lee, K.R. Shin, S. Namgung, B. Yoo and D.H. Shin, *Surf. Coat. Technol.*, 205 (2011) 3779.
14. O. Tazegul, F. Muhaffel, O. Meydanoglu, M. Baydogan, E.S. Kayali and H. Cimenoglu, *Surf. Coat. Technol.*, 258 (2014) 168.
15. L.X. Chen, Y. Liu, Z.Y. Liu, X.Y. Zhao and W. Li, *Mater. Corros.*, 66 (2015) 963.
16. M. Laleh, F. Kargar and A.S. Rouhaghdam, *J. Sol-Gel Sci. Technol.*, 59 (2011) 297.
17. V. Ezhilselvi, J.N. Balaraju and S. Subramanian, *Surf. Coat. Technol.*, 325 (2017) 270.
18. J.G. Qian, C. Wang, D. Li, B.L. Guo and G.L. Song, *Trans. Nonferrous Met. Soc. China*, 18 (2008) 19.
19. A. Bai and Z.J. Chen, *Surf. Coat. Technol.*, 203 (2009) 1956.
20. H.Y. Hsiao, P. Chung and W.T. Tsai, *Corrosion Sci.*, 49 (2007) 781.
21. A.L.K. Tan, A.M. Soutar, I.F. Annergren and Y.N. Liu, *Surf. Coat. Technol.*, 198 (2005) 478.
22. L.L. Chen, Y.H. Gu, L. Liu, S.J. Liu, B.B. Hou, Q. Liu and H.Y. Ding, *J. Alloy. Compd.*, 635 (2015) 278.
23. X.J. Cui, C.H. Liu, R.S. Yang, M.T. Li and X.Z. Lin, *Surf. Coat. Technol.*, 269 (2015) 228.
24. Z.U. Rehman, S.H. Shin, I. Hussain and B.H. Koo, *Surf. Coat. Technol.*, 307 (2016) 484.
25. A.L. Yerokhin, X. Nie, A. Leyland, A. Matthews and S.J. Dowey, *Surf. Coat. Technol.*, 122 (1999) 73.
26. Y.K. Pan, D.G. Wang and C.Z. Chen, *Mater. Lett.*, 119 (2014) 127.
27. F.H. Chung, *J. Appl. Cryst.*, 7 (1974) 519.
28. Y. Wang, J. Wang, J. Zhang and Z. Zhang, *Mater. Corros.*, 56 (2005) 88.
29. J.H. Dou, G.C. Gu and C.Z. Chen, *Mater. Lett.*, 196 (2017) 42.
30. J. Fontanella, C. Andeen and D. Schuele, *J. Appl. Phys.*, 45 (1974) 2852.
31. A.V. Hippel, *Trans. Fara. Soc.*, 42 (1946) 78.
32. J.M. Albella, I. Montero and J.M. Martinez-Duart, *Electrochim. Acta*, 32 (1987) 255.
33. W.P. Li, Z.Y. Qian, X.H. Liu, L.Q. Zhu and H.C. Liu, *Appl. Surf. Sci.*, 356 (2015) 581.
34. K.H. Dong, Y.W. Song, D.Y. Shan and E.H. Han, *Surf. Coat. Technol.*, 266 (2015) 188.
35. A.G. Rakoch, Y.V. Magurova, I.V. Bardin, G.M. El'khag, P.M. Zharinov and V.L. Kovalev, *Prot. Met.*, 44 (2008) 710.
36. A.K. Vijh, *Corrosion Sci.*, 11 (1971) 411.
37. M.Q. Pan, Y.J. Wang, T. Chen, J.Z. Liu, L.G. Chen and S.C. Di, *Adv. Mater. Res.*, 764 (2013) 21.
38. M. Stern and A.L. Geary, *J. Electrochem. Soc.*, 104 (1957) 56.

39. S.J. Lee, L.H.T. Do, J.L. Lee, C.Y. Chen and H.C. Peng, *Int. J. Electrochem. Sci.*, 13 (2018) 2705.
40. J.X. Han, Y.L. Cheng, W.B. Tu, T.Y. Zhan and Y.L. Cheng, *Appl. Surf. Sci.*, 428 (2018) 684.
41. M. Shokouhfar and S.R. Allahkaram, *Surf. Coat. Technol.*, 309 (2017) 767.
42. L. Guo, F. Zhang, L. Song, R.C. Zeng, S.Q. Li and E.H. Han, *Surf. Coat. Technol.*, 328 (2017) 121.
43. H.M. Wang and R. Akid, *Corrosion Sci.*, 49 (2007) 4491.
44. F. Mansfeld and M.W. Kendig, *J. Electrochem. Soc.*, 135 (1988) 828.
45. W.T. Yu, R.X. Sun, Z.Q. Guo, Z.Y. Wang, Y. He, G.Y. Lu, P.Y. Chen and K.Z. Chen, *Appl. Surf. Sci.*, 464 (2019) 708.
46. Q.Z. Chen, Z.Q. Jiang, S.G. Tang, W.B. Dong, Q. Tong and W.Z. Li, *Appl. Surf. Sci.*, 423 (2017) 939.
47. H.P. Duan, C.W. Yan and F.H Wang, *Electrochim. Acta*, 52 (2007) 3785.
48. N. Xiang, R.G. Song, H. Li, C. Wang, Q.Z. Mao and Y. Xiong, *J. Mater. Eng. Perform.*, 24 (2015) 5022.
49. D. Chen, R.Q. Wang, Z.Q. Huang, Y.K. Wu, Y. Zhang, G.R. Wu, D.L. Li, C.H Guo, G.R. Jiang, S.X. Yu, D.J. Shen and P. Nash, *Appl. Surf. Sci.*, 434 (2018) 326.
50. A. Hakimizad, K. Raeissi, M.A. Golozar, X.P. Lu, C. Blawert and M.L. Zheludkevich, *Surf. Coat. Technol.*, 324 (2017) 208.
51. F. Chen, Y.L. Zhang and Y. Zhang, *Int. J. Electrochem. Sci.*, 12 (2017) 6081.
52. R. Aliramezani, K. Raeissi, M. Santamaria and A. Hakimizad, *Surf. Coat. Technol.*, 329 (2017) 250.